Geophysical Research Letters

Supporting Information for

A composite seismic source model for the first major event during the 2022 Hunga (Tonga) volcanic eruption

Jinyin Hu[1,*], Thanh-Son Phạm[1] and Hrvoje Tkalčić[1]

[1]Research School of Earth Sciences, The Australian National University, Canberra, ACT, Australia

[*]Corresponding author: Jinyin Hu (jinyin.hu@anu.edu.au)

Contents of this file

Figures S1 to S15. Table S1 and S2.

S1. Results of synthetic experiments

The configuration of inversion is carefully designed for this study's synthetic experiments and real data application. We use the primitive parameterization of moment tensor, M_{ij} for the simplicity. When sampling the posterior, we manually scale up the Green's function according to prior knowledge of the event's scale moment to narrow down the parameters' dynamic ranges. Specifically, the Green's functions for MT and SF were multiplied by 10^{16} Nm and 10^{12} N, respectively. In all inversion, we define an uninformative prior within the [-2000, 2000] for all MT and SF source parameters. The prior time-shift parameters are set as [-12.5, 12.5] seconds to avoid the circle skipping because the waveforms are filtered into a 25-70 second band for a better signal to noise ratio. That of noise is set as [0, 400]. Additionally, we randomly initiated all walkers (i.e., 1200) of the affine invariance ensemble sampler (Goodman & Weare, 2010) in the prior hypercube and explored the parameter space by 6,000 iterations with each walker. Finally, the first half of the samples of each walker are discarded during the warm-up stage to ensure the remaining samples have reached the convergency, where all walkers fluctuate around the similar highest probability.

Table S1 and Figures S1-S9 are inversion results for the synthetic experiments. We use the same Earth's model to generate synthetics and perform inversions (i.e., without structural error) but still use the time-shifts to handle the waveform misalignment due to inappropriate assumptions of source types. We considered three input source mechanisms including an SF source (Case 1), an MT source (Case 2), and a composite source of the two (Case 3). In case 1, the input source only comprised of a downward force 5.0×10^{13} N. In Case 2, an explosive MT was used as the input, which was obtained from the real data MT inversion in Figure S11. In Case 3, we combined the two source types. As such, their contributions to the synthetic waveforms are comparable. All sources are fixed at a depth of 0.8 km, which is the depth of the caldera bottom post-eruption (see Section 2.3 for more details). For each input source scenario, we conducted three independent inversions assuming three unknown source types: MT-only inversion, SF-only inversion, and joint inversion, as summarized in Table S1. In each case, the unknown parameters include 3, 6, or 9 corresponding to the assumed source types, 8 station-specific noise parameters, and 16 time-shift parameters.

The inversion results for these synthetic scenarios are carefully verified. We follow the MT decomposition into double-couple (DC), isotropic (ISO), and compensated linear vector dipole (CLVD) components (Jost & Herrmann, 1989; Julian et al., 1998; Knopoff & Randall, 1970; Sipkin, 1986; Vavryčuk, 2015). We use the percentage of ISO, DC, and CLVD components after Vavryču (2001) and the moment magnitude to evaluate the recovered MT with the true MT. For the SF source, we directly compare the three force components. The contribution of one source type (e.g., SF or MT) to the observations is measured by the ratio of the peak-to-peak amplitude generated to that of observations. In the following, we discuss the details to support the three key points mentioned in the main text.

Firstly, we observe an ambiguity between the vertical force and isotropic MT. It can be theoretically explained by the similarity in the radiation pattern of surface waves from a vertical force and an ISO MT, as noted by Kanamori & Given (1982). In Case 1, where an SF was used as an input, the MT-only inversion resulted in a fake explosion solution with a 68.5% ISO component, which fits the waveforms with a reasonable VR of 65.5% (Figures S2b). Similarly, in Case 2, where an isotropic MT was used as the input, the SF-only inversion results in an upward force fitting the waveforms with a VR of 58.5% (Figure S4). The joint inversions for three cases (especially Cases 1 and 3) also indicated this tradeoff between a vertical force and ISO MT by a weak linear dependence between the vertical force component $\mathrm{F_z}$ and three diagonal MT elements, M_{xx}, M_{yy}, and M_{zz} (S3, S6, and S9). This tradeoff probably explains why SF-only inversion and MT-only inversion can individually generate reasonable solutions for this HTHH eruption in previous studies (Donner et al., 2023; Thurin & Tape, 2023; Thurin et al., 2022).

Second, for a composite source of MT and SF, SF- and MT-only inversion can only provide incomplete solutions, which may lead to a different explanation for the source process. In Case 3, both SF inversion and MT inversion provide the acceptable waveform fit VR of 79.3% and 84.9%, respectively, in Figures S7 and S8. In SF inversion, the SF solution is a near downward force with a dip angle of 85°(Figure S7b). The horizontal force components are to fit tangential components from the deviatoric MT part in the source. The recovered force is larger (~1.6 times) than the force in the true source because the extra vertical force is required to fit the waveform from the ISO MT part. In MT inversion, the MT solution is an explosive source whose ISO component is 6% higher than that in the input true source (Table S1). More ISO moment explains the waveforms from the vertical force when assuming the source is only an MT. Even though the SF and MT solutions already explain most of the waveforms individually, there are still unmodeled signals caused by inappropriate assumptions on source representation. Consequently, the recovered noise parameters are larger than the true value, i.e., three in this study (Figures S7b and S8b). Significant time-shifts are necessary to relax the search for source types further.

Third, the designed synthetic experiments demonstrate that the joint MT and SF inversion could reliably resolve different input source types. In the case of an input downward force (Case 1), the joint inversion explores widely the joint space of MT and SF as in Figure S3(a). Due to the tradeoff between vertical force and ISO noted above, an isotropic MT solution ($Mw = 5.94$) is recovered. However, its contribution to the waveforms is small (13%) compared with the SF part, as in Figure S3(d). The SF part of the solution is a downward force with a dip angle of 89.5°, (Figure S3c) and the force magnitude is $4.932 \times$ N, which is close to the input force of $5.0 \times$ N. The recovered MT+SF source gives a good waveform fit (VR=78%) between observations and predictions. Due to the shallow source depth in this experiment, i.e., 0.8 km, it is also difficult to distinguish an ISO from CLVD (e.g., Chiang et al., 2014; Ford et al., 2012; Kawakatsu, 1996; Hu et al., 2023), even though this ISO is a fake representation of the downward force. Therefore, a strip-shaped distribution appears on the source-type lune diagram (Tape & Tape, 2012) in dark colors in Figure S3(b).

A similar conclusion applies to the cases of the MT input source (Case 2) and the composite MT and SF input source (Case 3). In Case 2, the joint inversion performed as well as the MT inversion. The solution of the composite source suggests an MT rather than an SF solution because the SF part explains a small fraction of the synthetic waveforms (<<1.0%) in Figure S6. The recovered MT source is overlapped well with the input one on the lune diagram of source type in Figure S6(b). In Case 3, both MT and SF components are successfully retrieved by joint MT and SF inversion using a correct source representation from Table S1. The tradeoff between vertical force and three MT parameters, M_{xx}, M_{yy}, and M_{zz}, in Figure S9(a), is caused by the existence of vertical force.

The joint MT and SF inversions also recovered the noise amplitude and station-specific time-shifts in cases of three input sources (Figures S3d, S6d, and S9d). Note that the recovery was successful even when noisy data was involved. Take Case 1 as an example; all tangential components only contain added noise because the vertical force does not radiate tangential energy. In particular, the added noise on the tangential component of station G.PPTF is of relatively high amplitude. Joint MT and SF inversion retrieved the true input noise level of 3 at all stations. Besides, only small time-shifts are obtained because the true Earth's model is used, and the true source is recovered. Therefore, the joint MT and SF inversion provided a reliable solution for source parameters and free parameters in all three cases. Another set of synthetic tests using the input of the same MT components but with a directed upward force also supports this feasibility.

S2. Preparation for real data inversion

Table S2 and Figures S10 – S15 are inversion results for the first main event of the 2022 HTHH eruption (E1 in Figure 1b). Table S2 summarizes the results of six inversions. The data processing is based on the epicentral location 175.390°W, 20.546°S, and origin time of E1, 2022-01-15 04:14:45 UTC (USGS, 2022). We chose eight regional broadband stations in Figure 1(a). After correcting the instrument response, the raw data are converted into the vertical, radial, and tangential coordinate systems. Then, we filtered the waveforms between 25 and 70 seconds with a 4th-order Butterworth causal filter to obtain a better signal-to-noise ratio and to mitigate the structural error from the 1D Earth's assumption in this study. To reduce the correlation between data samples, the waveforms are down-sampled to 1 Hz and cut into a 200-s window centered on the surface wave signals (Figure S10). Predicted waveforms are calculated using Green's functions requested from the online database Syngine (Hutko et al., 2017) for the ak135f model (Montagner & Kennett, 1996), which was pre-computed by the axisymmetric spectra element code (AxiSEM – Nissen-Meyer et al., 2014) with the fixed depth at 0.8 km. Figures S11 – S15 expand the discussion briefly discussed in the main text.

Table S1: The summary of synthetic experiments. All sources are fixed at a depth of 0.8 km, which is the depth of the caldera bottom of post-eruption (see Section 2.3 for more details). Comparison between the true and recovered source is based on the variance reduction (VR) of waveform fit, ISO, DC and CLVD components of MT, moment magnitude, and three components of a SF. The numbers below each item in the top row are the true values. The unit of SF is 10^{12} N.

True source	**Inversion**	**VR**	**ISO** (54.6%)	**DC** (11.7%)	**CLVD** (33.7%)	$\mathbf{M_w}$ (6.21)	$\mathbf{F_x}$ (0)	$\mathbf{F_y}$ (0)	$\mathbf{F_z}$ (50)
Case 1: SF input	SF-only	78.1%	—	—	—	—	1.04	0.41	49.77
	MT-only	65.5%	68.5%	1.0%	30.5%	6.01	—	—	—
	MT+SF	78.0%	58.7%	2.1%	39.2%	5.94	0.28	0.36	49.30
Case 2: MT input	SF-only	58.5%	—	—	—	—	-6.49	-12.9	-49.34
	MT-only	84.9%	55.2%	11.2%	33.6%	6.20	—	—	—
	MT+SF	84.9%	55.3%	11.1%	33.6%	6.20	-1.13	-0.3	-1.42
Case 3: MT+SF input	SF-only	79.3%	—	—	—	—	-2.98	-5.69	73.96
	MT-only	84.9%	60.6%	4.5%	34.9%	6.25	—	—	—
	MT+SF	89.7%	55.5%	10.7%	33.8%	6.21	-0.63	0.57	49.22

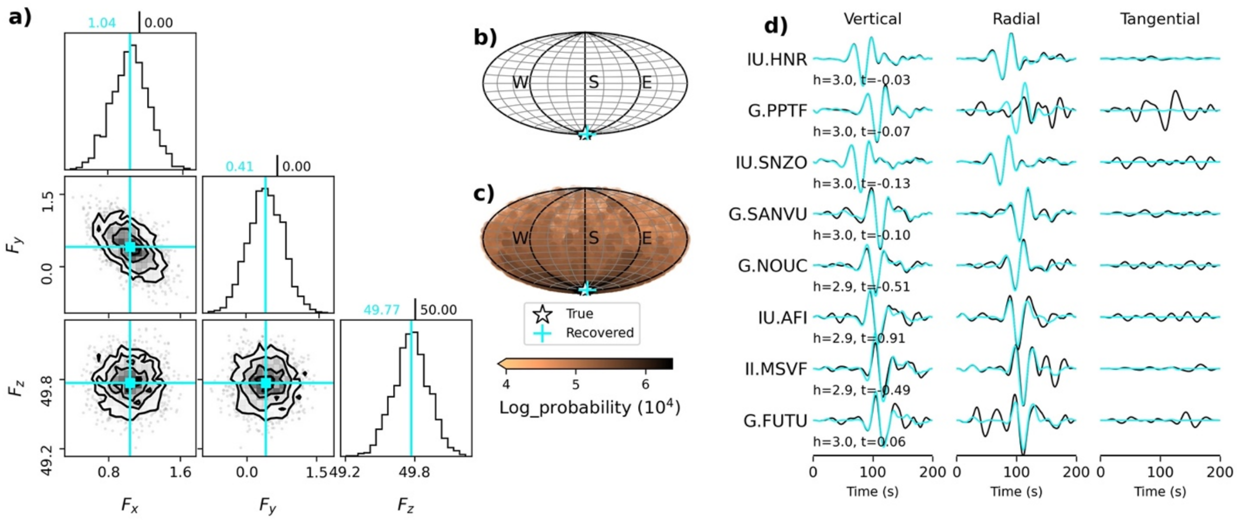

Figure S1: Results of SF-only inversion in the synthetic scenario when the true source is a downward force (Case 1). (a) The posterior distribution of three SF parameters. Cyan lines show the mean of each SF parameters corresponding the number in cyan above each column, separated from their true values in magenta by a vertical bar. (b) The diagram of the force orientations in convergency stage. The longitude and latitude correspond to force's azimuth and dip angle, respectively. (c) The diagram of the force orientations in whole inversion stage. The color bar displays log probability. (d) Fit between the 'observed' (black) and synthetic waveforms (cyan) obtained from the recovered SF solution. The numbers below each sub-panel are recovered station-specific noise parameter, and station-specific time shift, respectively. The true noise level and time-shift parameters are 3 and 0, respectively.

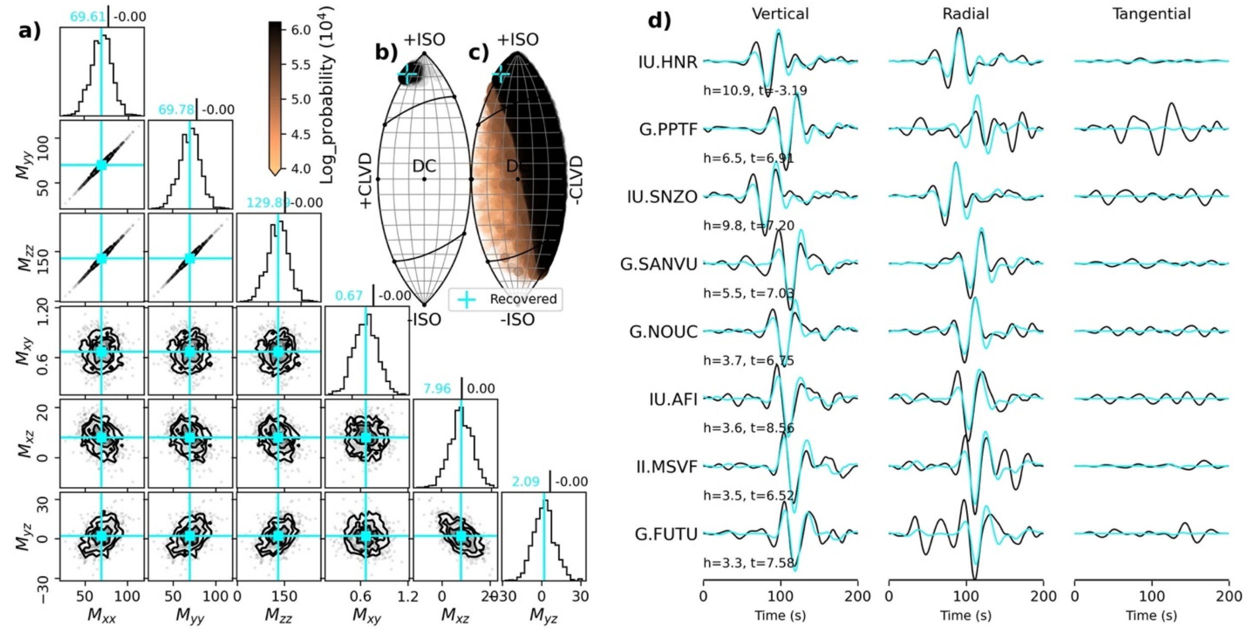

Figure S2: Results of MT-only inversion in the synthetic scenario when the true source is a downward force (Case 1). (a) The posterior distribution of six MT parameters. (b)The lune diagram with the converging MT solution from (a). The cyan cross shows the mean MT solution of the convergency stage, i.e., recovered MT. The color bar displays log probability. (c) The Lune source-type diagram shows the evolution of every MT solution during the entire inversion stage. (d) Fit between the 'observed' (black) and synthetic waveforms (cyan) obtained from the mean MT solution.

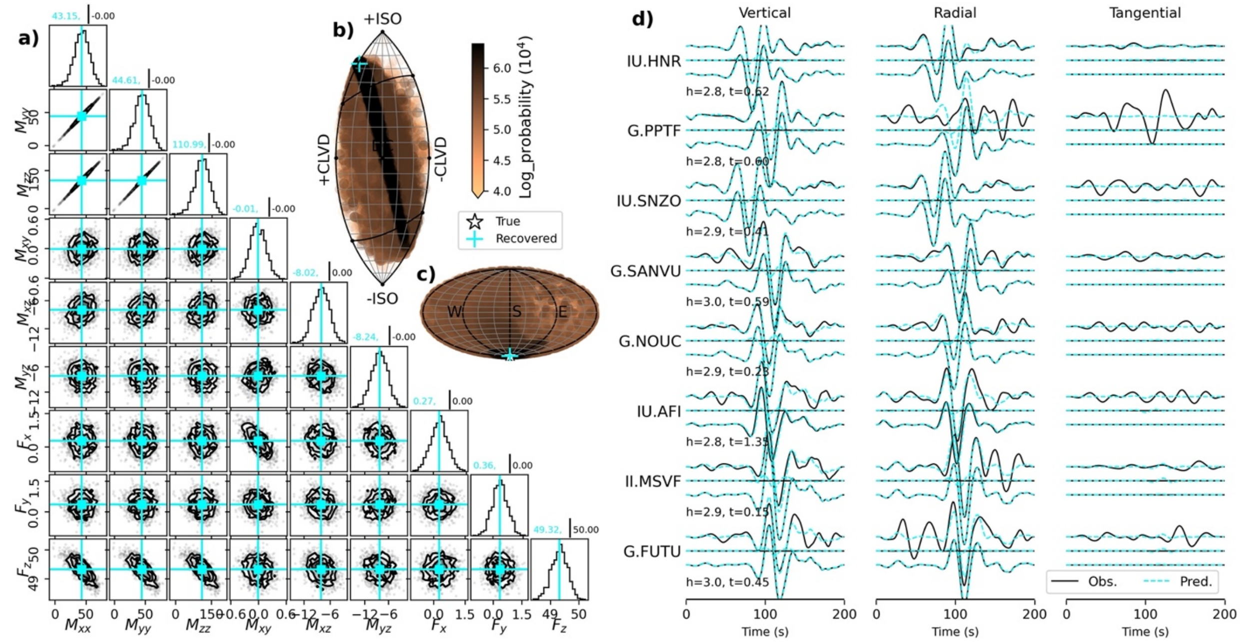

Figure S3: Results of joint MT and SF inversion in the synthetic scenario of Case 1. (a) Posterior distribution of the nine source parameters in the convergency stage of the inversion. The units of MT and SF parameters are 10^{16} Nm, 10^{12} N, respectively. (b)The lune diagram with the all MT solutions in the entire inversion stage. (c) The diagram of force orientation during the entire inversion stage. The longitude and latitude correspond to force's azimuth and dip angle, respectively. (d) Waveform fit between observations (black) and predictions (cyan).

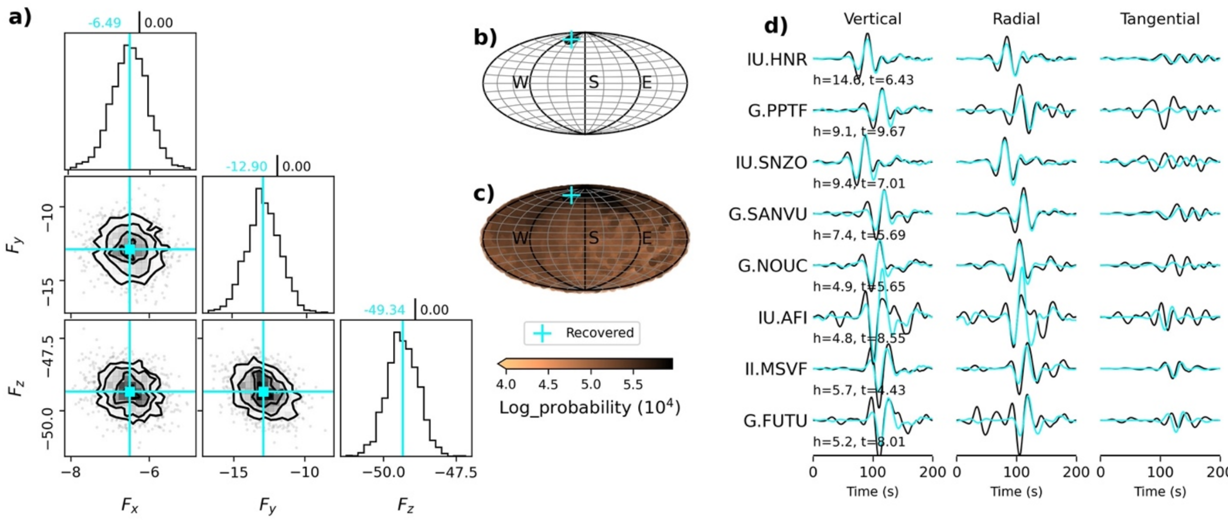

Figure S4: Results of SF-only inversion in the synthetic scenario when the true source is a MT (Case 2). See caption of Figure S1 for more details.

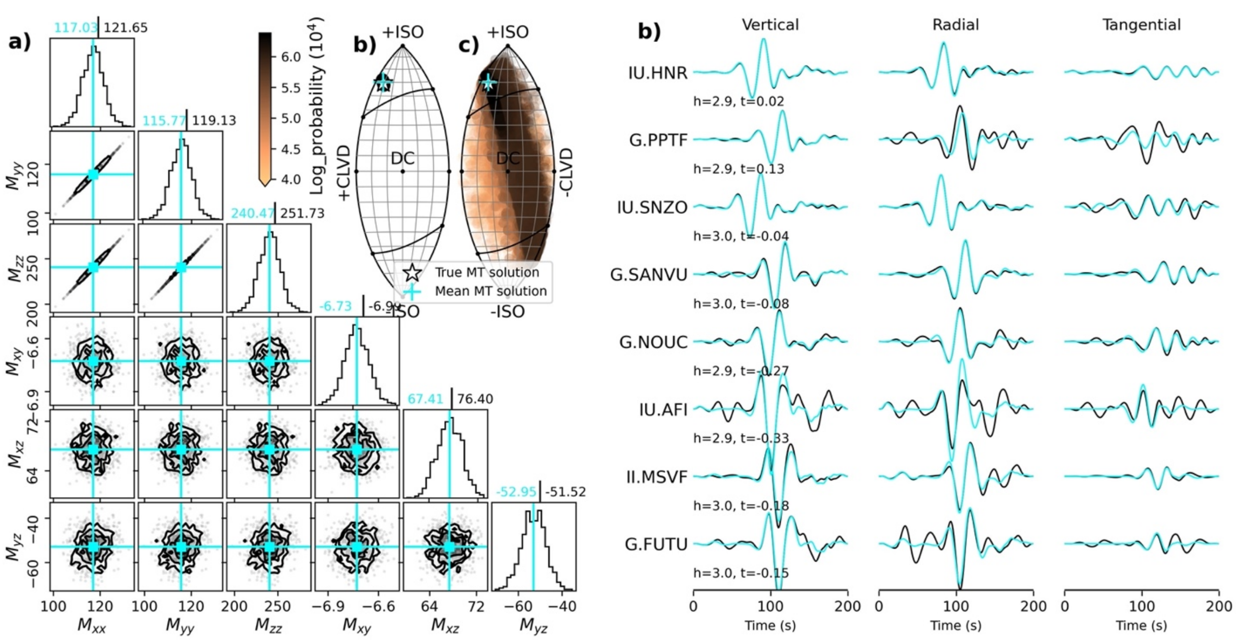

Figure S5: Results of MT-only inversion in the synthetic scenario when the true source is a MT (Case 2). See caption of Figure S2 for more details.

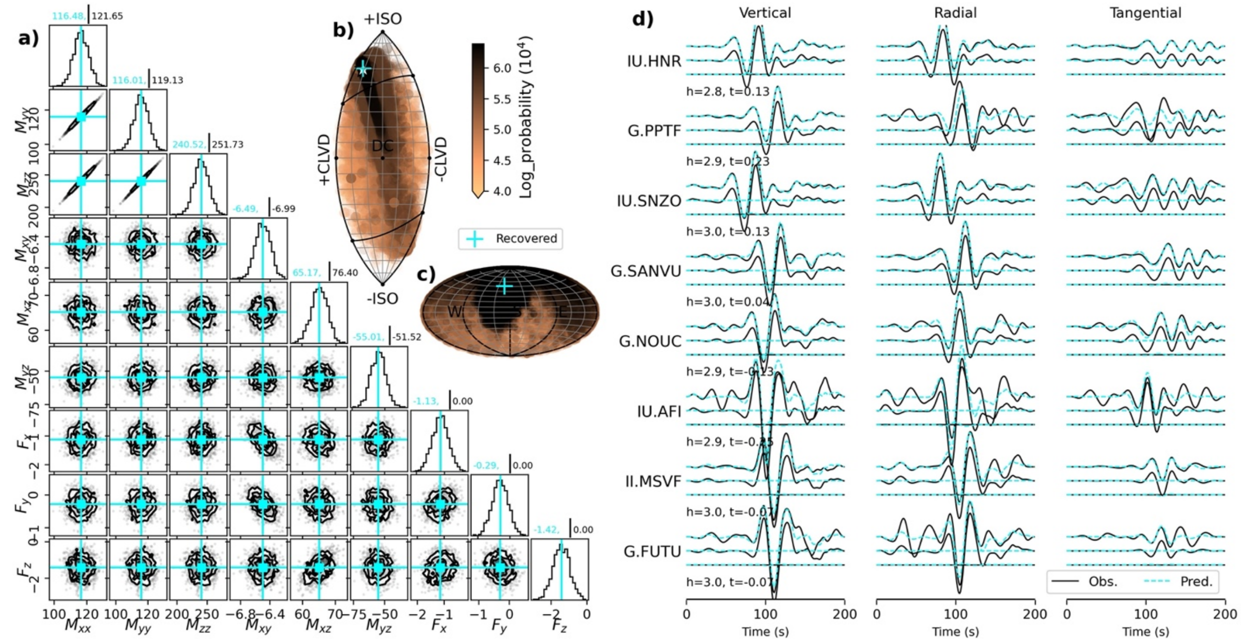

Figure S6: Results of joint MT and SF inversion in the scenario of Case 2. The white stars in (b) is the true MT input. See the caption of Figure S3 for more details.

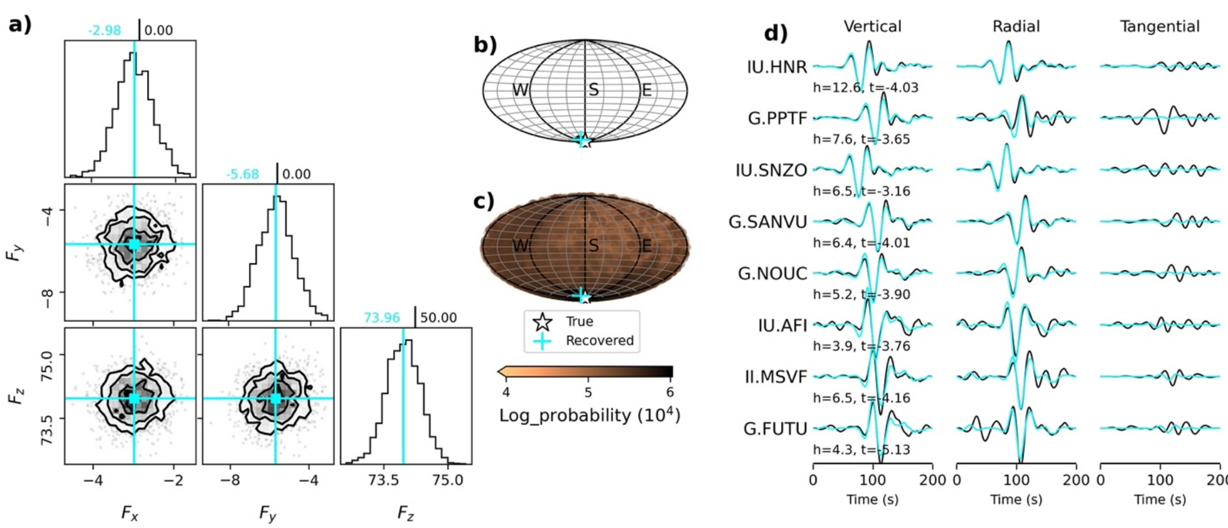

Figure S7: Results of SF-only inversion in the synthetic scenario when the true source is a composite of MT and downward SF (Case 3). See caption of Figure S1 for more details.

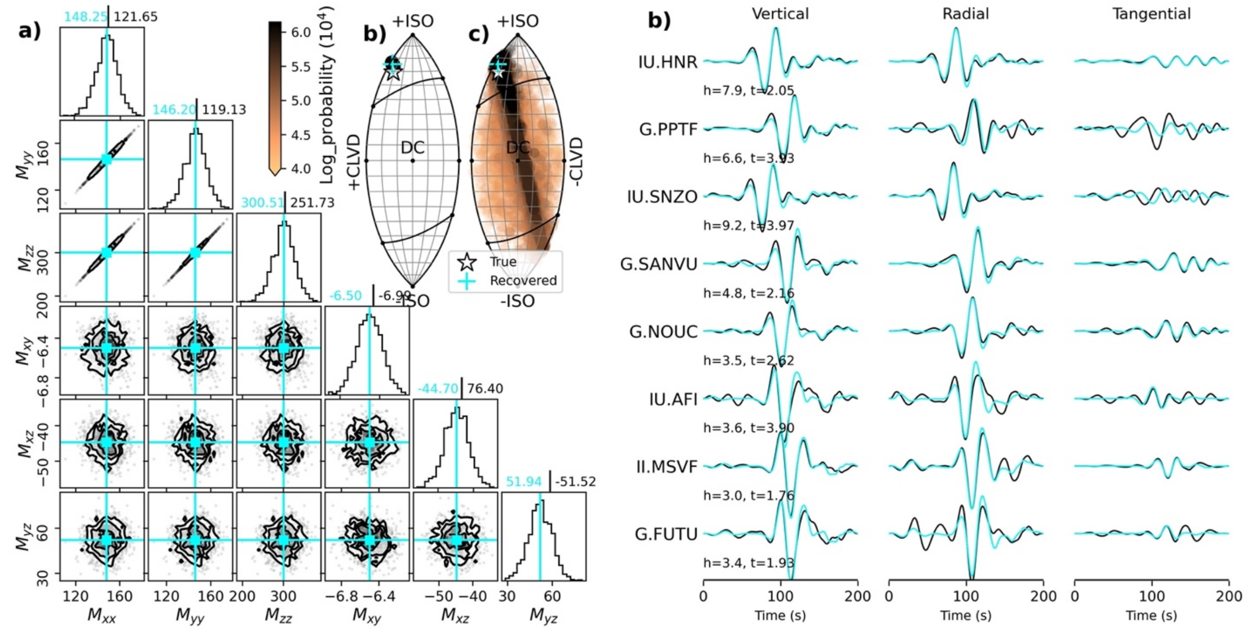

Figure S8: Results of MT-only inversion in the synthetic scenario when the true source is a composite of MT and downward SF (Case 3). See caption of Figure S2 for more details.

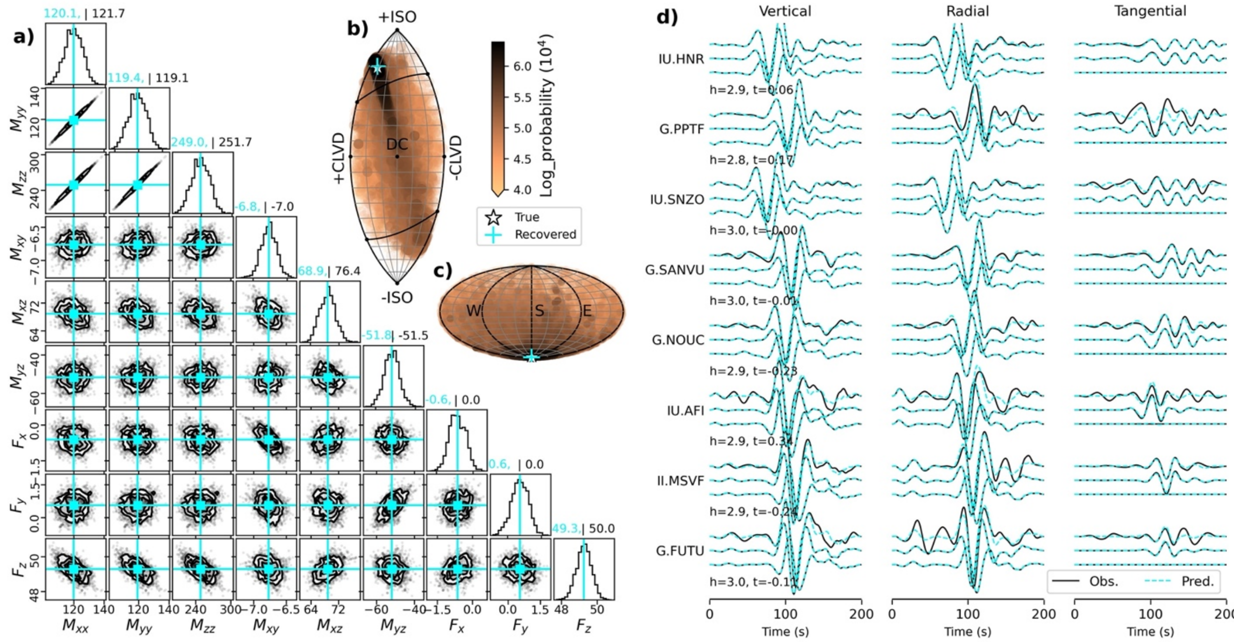

Figure S9: Results of joint MT and SF inversion in the synthetic scenario when the true source is a composite of MT and downward SF (Case 3). See caption of Figure S3 for more details.

Table S2: Comparison between six solutions for the real data of E1 from SF-only inversion, MT-only inversion and joint MT and SF inversion. The unit of SF is 10^{12} N.

Inversion	**VR**	**ISO**	**DC**	**CLVD**	$\mathbf{M_w}$	$\mathbf{F_x}$	$\mathbf{F_y}$	$\mathbf{F_z}$
Fz-only	53.8%	—	—	—	—	—	—	47.7
SF-only	55.1%	—	—	—	—	-13.48	-2.83	48.03
MT-only	76.7%	58.1%	7.4%	34.5%	6.22	—	—	—
ISO+SF	67.6%	100%	—	—	5.59	-12.57	-2.06	-27.4
MT+Fz	77.3%	62.5	5.6%	31.9%	6.26	—	—	-18.27
MT+SF	78.5%	62.4%	6.9%	30.7%	6.25	3.58	1.9	-20.17

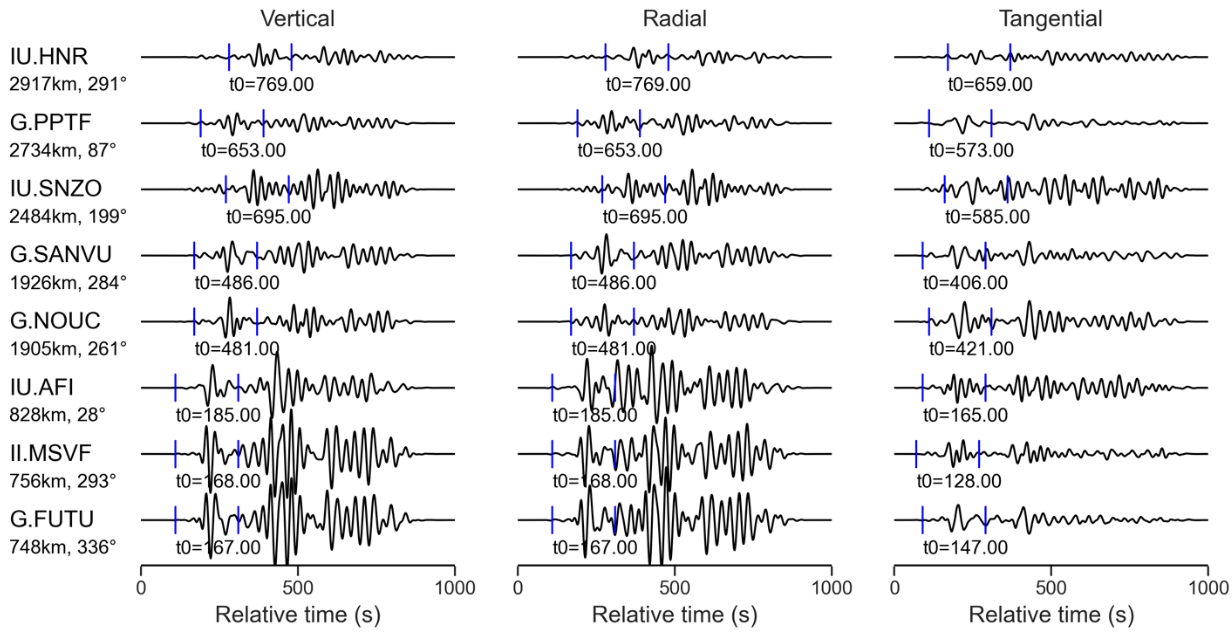

Figure S10. The waveforms of the 2022 HTHH eruption. The data is fieltered between 25 – 70 second. The time zero correponds to the S-wave arrival time in ak135f model (Montagner & Kennett, 1996). The two blue lines at each component show the start time and end time of the 200s-window used in the inversion for E1 event. The number $t0$ denotes the start time of the window from the origin time.

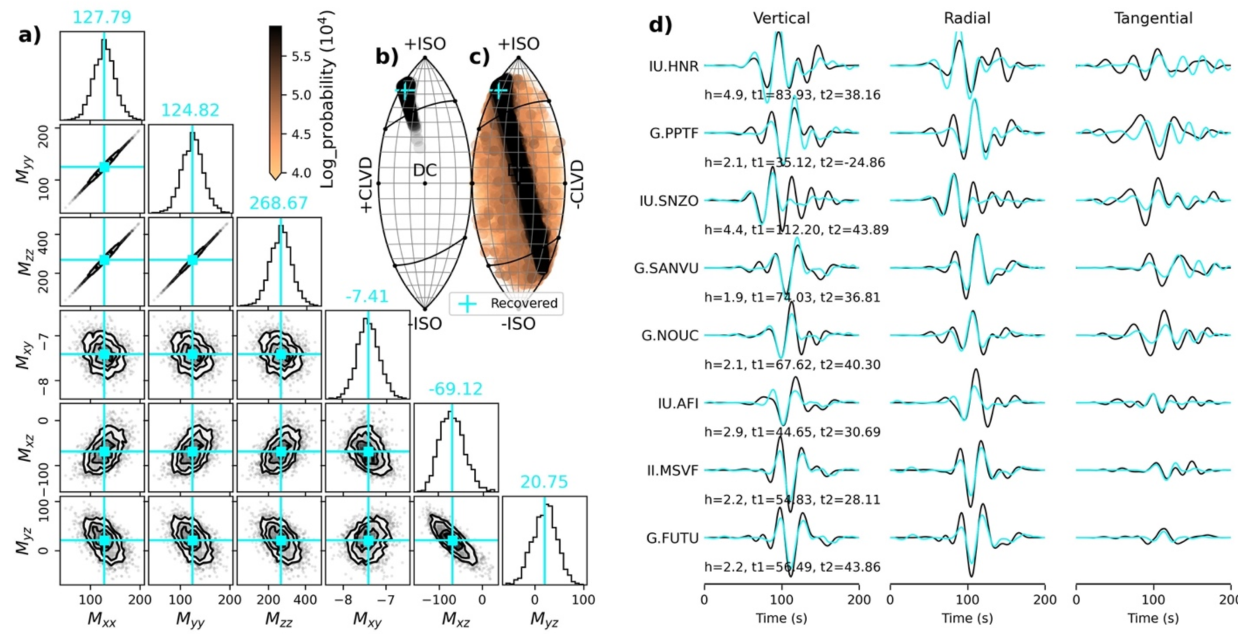

Figure S11. Results of MT-ony inversion for the 2022 HTHH first main eruption. (a) The posterior distribution of six MT parameters. Cyan lines show the mean of each MT parameters corresponding the number in cyan above each column. Three parameters of the MT, M_{xx}, M_{yy}, and M_{zz}, show a strong linear dependency on each other which is caused by the ISO-CLVD tradeoff for shallow explosive sources (Hu et al., 2023). (b) MT evolution in the convergency stage. (c) MT evolution in the whole inversion stage. (d) Fit between the observed (black) and synthetic waveforms (cyan) obtained from the mean MT solution.

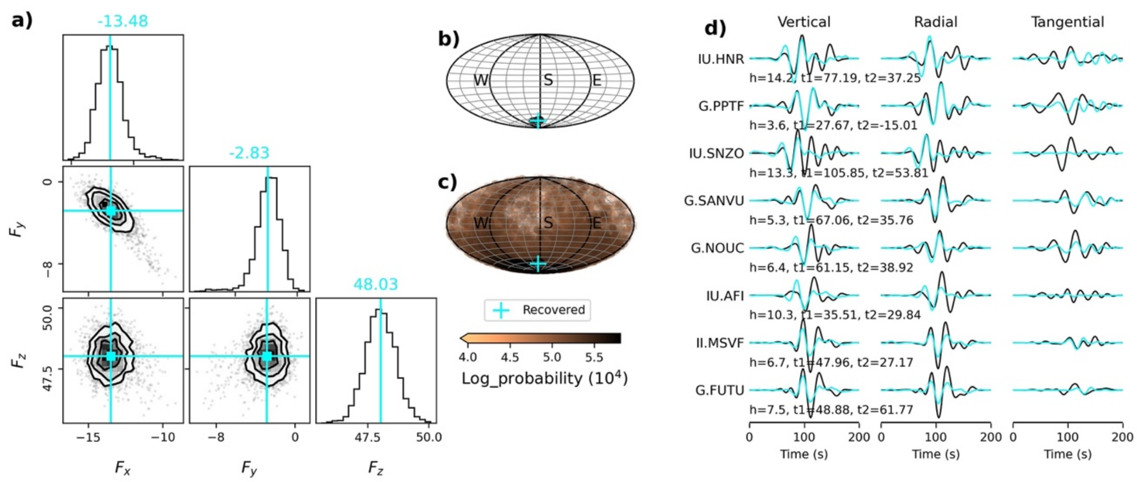

Figure S12. Results of SF-only inversion for the 2022 HTHH first main eruption. (a) The posterior distribution of three SF parameters. Cyan lines show the mean of each force parameter corresponding the number in cyan above each column. (b) The diagram of the force orientations in convergency stage. The longitude and latitude correspond to force's azimuth and dip angle, respectively. (c) The diagram of the force orientations in entire inversion stage. The color bar displays log probability. (d) Fit between the observed (black) and synthetic waveforms (cyan) obtained from the mean SF solution which are shown in cyan in (a). The numbers below each sub-panel are recovered station-specific noise parameter, and station-specific time shift for vertical/radial t_1 and tangential components t_2, respectively.

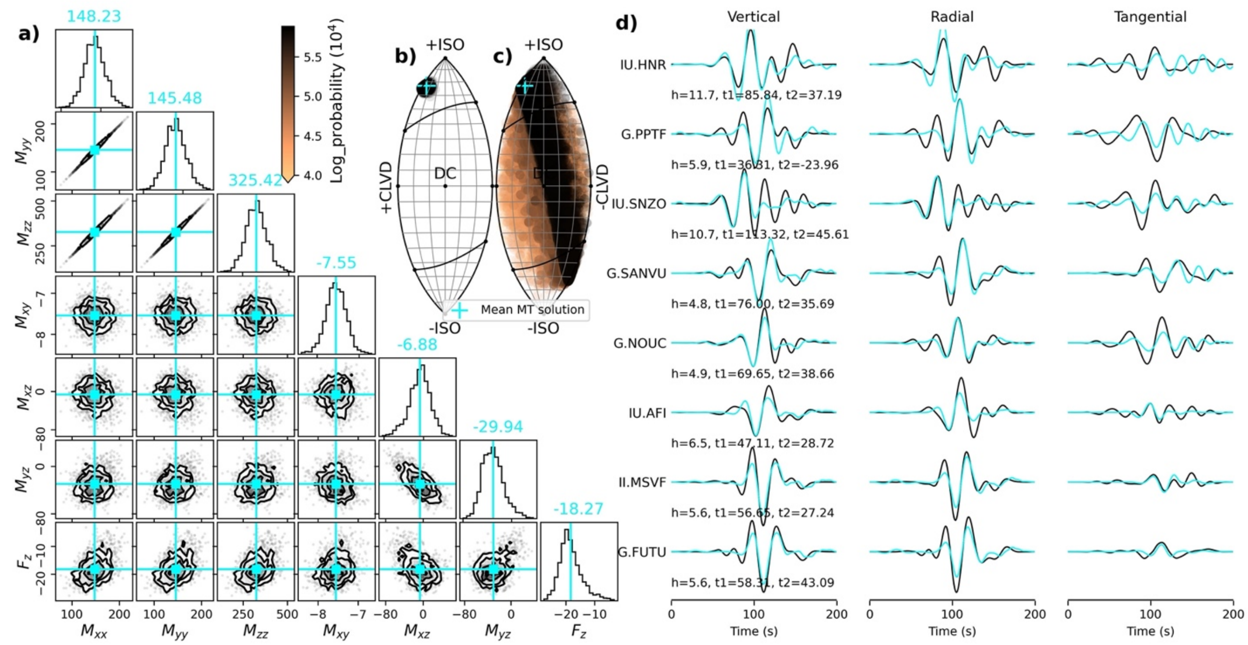

Figure S13: Results of joint MT and vertical force Fz inversion for the 2022 HTHH first main eruption. See the caption of Figure S11 for more details.

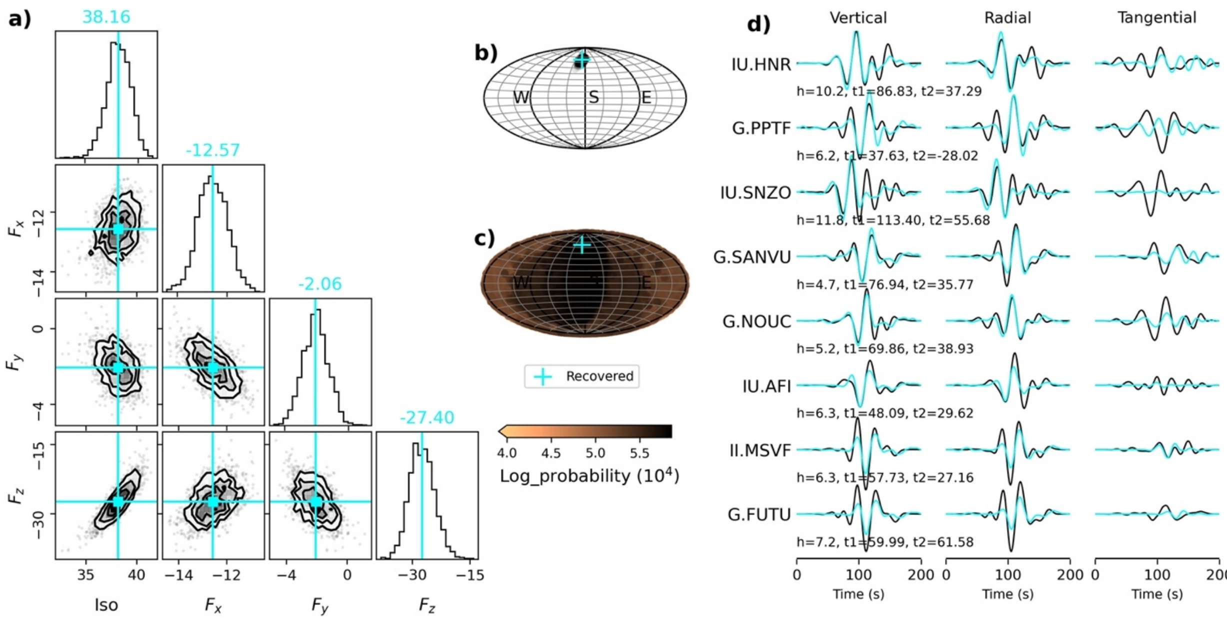

Figure S14: Result of joint ISO and SF inversion for the 2022 HTHH first main eruption. (a) The posterior distribution of four source parameters. Cyan lines show the mean of each parameter corresponding to the number in cyan above each column. (b) The diagram of the force orientations in convergency stage. The longitude and latitude correspond to force's azimuth and dip angle, respectively. (c) The diagram of the force orientations in entire inversion stage. The color bar displays log probability. (d) Fit between the observed (black) and synthetic waveforms (cyan) obtained from the mean MT solution.

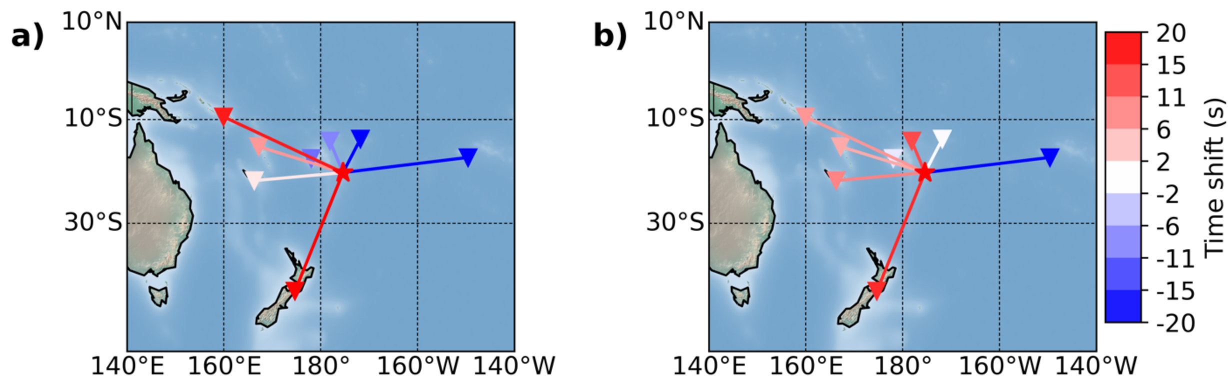

Figure S15: Recovered station-specific time shifts for (a) Rayleigh waves (vertical and radial components), and (b) for Love waves (tangential component).

References

Chiang, A., Dreger, D. S., Ford, S. R., & Walter, W. R. (2014). Source Characterization of Underground Explosions from Combined Regional Moment Tensor and First-Motion Analysis. *Bulletin of the Seismological Society of America*, *104*(4), 1587–1600. https://doi.org/10.1785/0120130228

Donner, S., Steinberg, A., Lehr, J., Pilger, C., Hupe, P., Gaebler, P., et al. (2023). The January 2022 Hunga Volcano explosive eruption from the multitechnological perspective of CTBT monitoring. *Geophysical Journal International*, *235*(1), 48–73. https://doi.org/10.1093/gji/ggad204

Ford, S. R., Walter, W. R., & Dreger, D. S. (2012). Event Discrimination using Regional Moment Tensors with Teleseismic-P Constraints. *Bulletin of the Seismological Society of America*, *102*(2), 867–872. https://doi.org/10.1785/0120110227

Goodman, J., & Weare, J. (2010). Ensemble samplers with affine invariance. *Communications in Applied Mathematics and Computational Science*, *5*(1), 65–80. https://doi.org/10.2140/camcos.2010.5.65

Hu, J., Phạm, T.-S., & Tkalčić, H. (2023). Seismic moment tensor inversion with theory errors from 2-D Earth structure: implications for the 2009–2017 DPRK nuclear blasts. *Geophysical Journal International*, *235*(3), 2035–2054. https://doi.org/10.1093/gji/ggad348

Hutko, A. R., Bahavar, M., Trabant, C., Weekly, R. T., Fossen, M. V., & Ahern, T. (2017). Data Products at the IRIS-DMC: Growth and Usage. *Seismological Research Letters*, *88*(3), 892–903. https://doi.org/10.1785/0220160190

Jost, M. L., & Herrmann, R. B. (1989). A Student's Guide to and Review of Moment Tensors. *Seismological Research Letters*, *60*(2), 37–57. https://doi.org/10.1785/gssrl.60.2.37

Julian, B. R., Miller, A. D., & Foulger, G. R. (1998). Non-double-couple earthquakes 1. Theory. *Reviews of Geophysics*, *36*(4), 525–549. https://doi.org/10.1029/98RG00716

Kanamori, H., & Given, J. W. (1982). Analysis of long-period seismic waves excited by the May 18, 1980, eruption of Mount St. Helens—A terrestrial monopole? *Journal of Geophysical Research: Solid Earth*, *87*(B7), 5422–5432. https://doi.org/10.1029/JB087iB07p05422

Kawakatsu, H. (1996). Observability of the isotropic component of a moment tensor. *Geophysical Journal International*, *126*(2), 525–544. https://doi.org/10.1111/j.1365-246X.1996.tb05308.x

Knopoff, L., & Randall, M. J. (1970). The compensated linear-vector dipole: A possible mechanism for deep earthquakes. *Journal of Geophysical Research (1896-1977)*, *75*(26), 4957–4963. https://doi.org/10.1029/JB075i026p04957

Montagner, J.-P., & Kennett, B. L. N. (1996). How to reconcile body-wave and normal-mode reference earth models. *Geophysical Journal International*, *125*(1), 229–248. https://doi.org/10.1111/j.1365-246X.1996.tb06548.x

Nissen-Meyer, T., van Driel, M., Stähler, S. C., Hosseini, K., Hempel, S., Auer, L., et al. (2014). AxiSEM: broadband 3-D seismic wavefields in axisymmetric media. *Solid Earth*, *5*(1), 425–445. https://doi.org/10.5194/se-5-425-2014

Sipkin, S. A. (1986). Interpretation of non-double-couple earthquake mechanisms derived from moment tensor inversion. *Journal of Geophysical Research: Solid Earth*, *91*(B1), 531–547. https://doi.org/10.1029/JB091iB01p00531

Tape, W., & Tape, C. (2012). A geometric setting for moment tensors: A geometric setting for moment tensors. *Geophysical Journal International*, *190*(1), 476–498. https://doi.org/10.1111/j.1365-246X.2012.05491.x

Thurin, J, & Tape, C. (2023). Comparison of force and moment tensor estimations of subevents during the 2022 Hunga-Tonga submarine volcanic eruption. *Geophysical Journal International*, ggad323. https://doi.org/10.1093/gji/ggad323

Thurin, Julien, Tape, C., & Modrak, R. (2022). Multi-Event Explosive Seismic Source for the 2022 Mw 6.3 Hunga Tonga Submarine Volcanic Eruption. *The Seismic Record*, *2*(4), 217–226. https://doi.org/10.1785/0320220027

USGS. (2022). M 5.8 Volcanic Eruption - 68 km NNW of Nukuʻalofa, Tonga. Retrieved November 3, 2023, from https://earthquake.usgs.gov/earthquakes/eventpage/us7000gc8r/executive

Vavryčuk, V. (2001). Inversion for parameters of tensile earthquakes. *Journal of Geophysical Research: Solid Earth*, *106*(B8), 16339–16355. https://doi.org/10.1029/2001JB000372

Vavryčuk, V. (2015). Moment tensor decompositions revisited. *Journal of Seismology*, *19*(1), 231–252. https://doi.org/10.1007/s10950-014-9463-y